

Visualizing single molecules inside living cells using total internal reflection fluorescence microscopy

G.I. Mashanov,^a D. Tacon,^b A.E. Knight,^a M. Peckham,^b and Justin E. Molloy^{c,*}

^a *Biology Department, University of York, Heslington, York YO1 5DD, UK*

^b *School of Biomedical Science, Leeds University, Leeds LS2 9JT, UK*

^c *National Institute for Medical Research, The Ridgeway, Mill Hill, London NW7 1AA, UK*

Accepted 15 October 2002

Abstract

Over the past 10 years, advances in laser and detector technologies have enabled single fluorophores to be visualized in aqueous solution. Here, we describe methods based on total internal reflection fluorescence microscopy (TIRFM) that we have developed to study the behavior of individual protein molecules within living mammalian cells. We have used cultured myoblasts that were transiently transfected with DNA plasmids encoding a target protein fused to green fluorescent protein (GFP). Expression levels were quantified from confocal images of control dilutions of GFP and cells with 1–100 nM GFP were then examined using TIRFM. An evanescent field was produced by a totally internally reflected, argon ion laser beam that illuminated a shallow region (50–100 nm deep) at the glass–water interface. Individual GFP-tagged proteins that entered the evanescent field appeared as individual, diffraction-limited spots of light, which were clearly resolved from background fluorescence. Molecules that bound to the basal cell membrane remained fixed in position for many seconds, whereas those diffusing freely in the cytoplasm disappeared within a few milliseconds. We developed automated detection and tracking methods to recognize and characterize the behavior of single molecules in recorded video sequences. This enabled us to measure the kinetics of photobleaching and lateral diffusion of membrane-bound molecules.

© 2003 Elsevier Science (USA). All rights reserved.

Keywords: Single molecule; Total internal reflection fluorescence microscopy; TIRF; GFP imaging; Live-cell imaging

1. Introduction

1.1. Seeing single molecules inside living cells

The goal of the work described here is to measure the dynamic behavior of individual protein molecules within a live mammalian cell that is grown in culture. We wish to observe how proteins are distributed in a cell, the structures that they are associated with, how rapidly they move, bind, and unbind, and how these properties are affected by different signaling pathways. Clearly, these are bold aims; however, many researchers are now trying to address such questions using single-molecule

approaches and it is likely that significant progress will be made toward such goals in the near future [1–10].

In this paper, we describe how single fluorophores can be observed directly at the internal plasma membrane of living mouse myoblast cells and how images can be analyzed automatically so that the temporal and spatial trajectories of many individual fluorophores can be determined.

1.2. Theoretical framework and basis for the technique

If the bulk concentration of a fluorophore is in the nanomolar range, then there will be approximately one molecule per cubic micrometer. If an optical sectioning technique is used, then individual fluorophores should be visible as separate spots of light. For this to form an experimental system, the source of exciting light must be sufficiently intense and the optical detector system suit-

* Corresponding author. Fax: +44-208-906-4419.

E-mail address: jmolloy@nimr.mrc.ac.uk (J.E. Molloy).

ably sensitive to enable images to be captured at video rate. Successful development of a new method such as this requires consideration of where compromises must be made. Careful consideration needs to be used to decide when either appropriate or best precision are needed. Measurements with best precision may be at the physical limit so that compromises must be made between certain physical parameters, e.g., between time-resolution and signal-to-noise ratio. In the following section, we discuss some of the physical limits to single-molecule detection (e.g., how many photons a single fluorophore emits before it photobleaches) and some of the systematic limitations that need to be dealt with (e.g., background autofluorescence intrinsic to living cells). In our experiments, we wish to observe single proteins moving inside a living cell. To achieve this, we express them as fusion constructs with green fluorescent protein (GFP). The beauty of this approach is that any protein (or protein domain) can be specifically tagged and its localization observed within a live cell with minimal intervention [11]. However, some disadvantages should be considered: GFP is a fairly large fluorescent tag (27 kDa molecular weight [12]) and may therefore interfere with normal functioning of the protein under study; expression of a fluorescently tagged protein usually results in overexpression of the protein in the cell, which may affect cell behavior and/or function; GFP fluorescence is excited by blue light (around 488 nm), which causes other substances in a living cell to fluoresce; and, along with normal photobleaching processes, GFP also exhibits temporary “blinking” and “switching” behaviors [13] which complicate interpretation of kinetic data.

We have used a mutant isoform of GFP (eGFP; GFP-65T [14]) that has superior excitation and emission properties compared to those of wild-type GFP. This isoform is excited at 488 nm and emits at 510 nm. Its fluorescence lifetime is about 3.2 ns [15] and so emission saturation should occur at 3×10^8 photons per second; however, measured values are closer to $8.5 \times 10^6 \text{ s}^{-1}$, probably because of a slower, competing, deexcitation mechanism [16]. Using 488-nm light, excitation saturation occurs at an incident intensity of 29 kW cm^{-2} [16] (i.e., $29 \times 10^3/h\nu = 7.2 \times 10^{22} \text{ photons s}^{-1} \text{ cm}^{-2}$, and if quantum efficiency = 60% and absorption cross section = 1.9 \AA^2 this gives the observed output of $8.5 \times 10^6 \text{ photons s}^{-1} \text{ fluorophore}^{-1}$). At saturating excitation the average time to photobleaching is about 4 ms [16] and shows monoexponential behavior, giving 30,000 photons output per fluorophore before photobleaching. At lower excitation intensities both average emission rate and time to photobleaching increase linearly with excitation power.

From a practical standpoint, excitation intensity (e.g., laser power) should be adjusted to give an emission rate and a fluorophore lifetime that is appropriate to the

type of information required. Photon counting statistics, noise level, and mean time to photobleaching all interact in a somewhat competing manner. To observe slow processes, low powers should be used to increase the average time until photobleaching. Fast processes require high laser power to increase the photon emission rate so that fast data collection is possible.

Next, we need to consider how a single fluorophore can be imaged in three-dimensional specimens such as living cells. Standard epifluorescence microscopy is usually unsuitable because fluorophores throughout the thickness of the specimen produce out-of-focus background noise due to poor *z*-axis discrimination [17]. Instead, a form of optical sectioning is required: either confocal microscopy or total internal reflection fluorescence microscopy (TIRFM) [18]. For our studies, TIRFM is the method of choice because it enables a very thin section (<100 nm) to be viewed continuously as a wide-field (i.e., non-scanned) image. This means that individual fluorophores that enter the evanescent field can be seen as separate, diffraction-limited spots and that background fluorescence from out-of-focus fluorophores and cell autofluorescence (mainly from flavonoids) is minimized.

1.3. TIRFM

When light travels from a high- to a low-refractive-index medium (e.g., $n_1 = 1.51$ for glass, $n_2 = 1.33$ for water), striking the interface at an angle that exceeds the so-called “critical” angle, θ_c , a phenomenon termed total internal reflection (TIR) occurs. The light path between two such media is given by Snell’s law: $\sin(i)/\sin(r) = n_2/n_1$ (where *i* is incident angle, *r* is refracted angle, and n_1 and n_2 are refractive indices). If $(n_2/n_1)/\sin(i) \geq 1$ then *r* must exceed 90° and light cannot pass into the second medium. The critical angle for total internal reflection, $\theta_c = \arcsin(n_2/n_1)$, is equal to 62° for a glass–water interface (Fig. 1a). Importantly, in the region where the light beam is reflected, an evanescent electric field is generated at the optical frequency. The evanescent field penetrates the optically less dense medium (e.g., water) with an exponentially decaying intensity, that falls by a factor, $1/e$, just 100 nm from the interface [19]. Because the evanescent field is restricted to the region of the interface, fluorescent molecules will be excited only if they happen to enter the field. TIRFM exploits this principle and is ideal for studying fluorescent molecules inside living cells that are cultured in an aqueous medium on glass or quartz microscope coverslips.

2. Description of the methods

There are two main types of TIR illumination: the prism-coupled method in which either a prism or a cy-

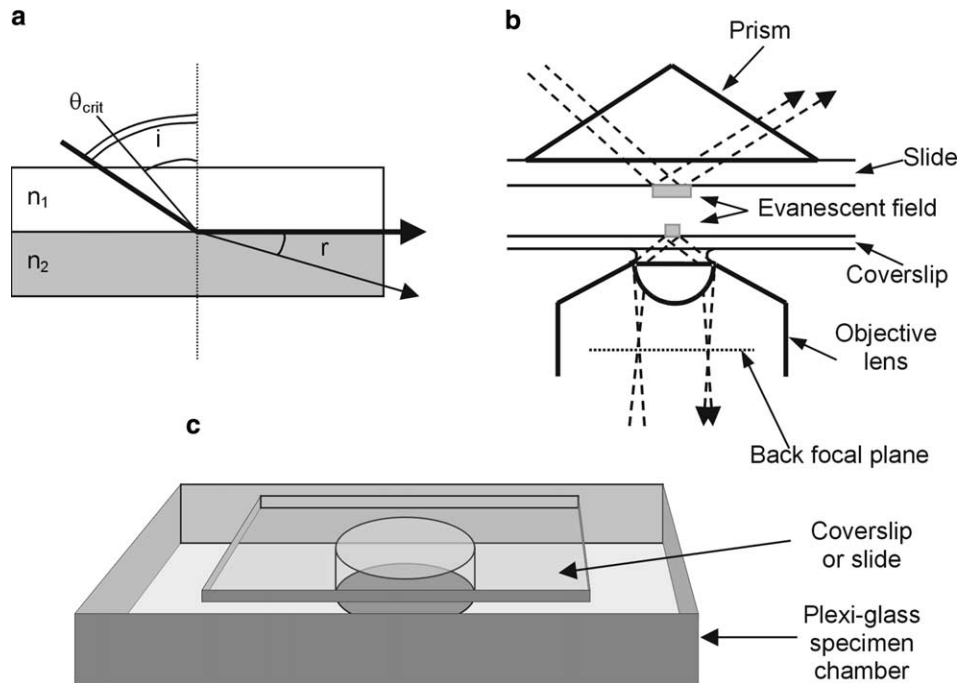


Fig. 1. (a) Total internal reflection occurs when light traveling from a high- to a low-refractive-index medium (e.g., $n_1 = 1.47$ for quartz, $n_2 = 1.3$ for water) strikes the interface at an angle that exceeds the so-called “critical” angle, θ_c . We know that the light path between two such media is given by Snell’s law, $\sin(i)/\sin(r) = n_2/n_1$ (where i is incident angle, r is refracted angle, and n_1 and n_2 are refractive indices), and can infer that if $(n_2/n_1)/\sin(i) \geq 1$ then r must exceed 90° and light cannot then pass into the second medium. The critical angle for total internal reflection, $\theta_c = \arcsin(n_2/n_1)$ is equal to 62° for a glass–water interface. (b) Two types of TIRFM are shown. (Top) Prism-based method, in which a prism or a hemicylindrical lens is used to couple the incident light into the specimen. Here a prism is coupled to the microscope slide using immersion oil. Note that the prism is mounted on the side opposite to that of the objective lens, illustrated here as for an inverted microscope (see Fig. 2 for a detailed description of the optical circuit). (Bottom) Objective lens-based method, in which incident light is focused at the outer-most edge of the back focal plane of a high-numerical-aperture (NA) objective lens (e.g., Zeiss $100\times$ Fluor 1.45 NA) (see Fig. 3 for a detailed description of the optical circuit). (c) A typical live cell imaging flow-cell chamber is shown. This would be filled with a suitable bathing medium; a laser beam (at $>\theta_c$ incident angle) and cell are shown (not to scale).

lindrical lens is used to introduce the light beam from the side opposite the objective lens (Fig. 1b, top) and the objective lens-coupled method in which the input laser beam is focused at the very edge of the back focal plane of a high-numerical-aperture ($NA > 1.33$) objective lens (Fig. 1b, bottom). The two TIR methods are described briefly here, together with a detailed description of our setup which we have optimized for studying single molecules inside live cultured cells (see Section 3).

2.1. Prism-coupled method

This method is easy to build and align and standard optical components made from quartz (both prism and slide) can be used (optical components, e.g., prisms, lenses, and mirror, were obtained from Comar Optical, Cambridge, UK). Use of a hemicylindrical lens or a simple prism enables the incident beam to be coupled into the glass–water interface. Using a suitably positioned lens to focus the laser at the specimen plane, a mirror or laser fixed on a translation mount enables the TIR angle to be adjusted without moving the illumination region (see Fig. 2 for details). An optical bread-

board or optical table with a rail mounting system enables components to be manually adjusted over large ranges and adjustable component mounts provide fine position control (mechanical components were sourced from Elliot Scientific, Harpenden, UK). The main disadvantage of this method, especially for single-molecule detection inside cells, is that the objective lens is placed on the side of the sample opposite to that of the evanescent field. This means that either the sample must be very thin ($<20\ \mu\text{m}$) or a water-immersion objective lens must be used. However, the method gives a very good contrast ratio because the incident laser beam does not travel through the objective lens (see following section).

2.2. Objective lens-coupled method

This method [20,21] requires use of a high-numerical-aperture objective lens ($NA > 1.3$) and works by exploiting the fact that the outer perimeter of such lenses cause light to approach the specimen at greater than the critical angle (Fig. 3). We have found that a lens with numerical aperture 1.45 can be used satisfactorily as the angle of incident light from the peripheral region (74°)

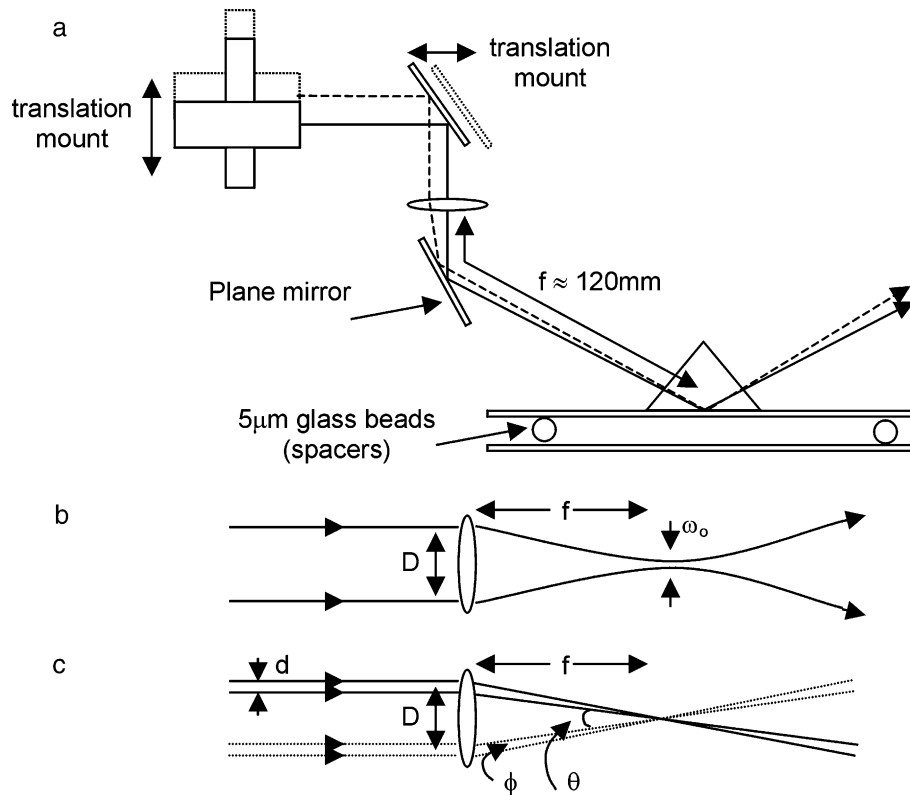


Fig. 2. (a) Optical circuit used to produce prism-coupled total internal reflection fluorescence. An argon ion or solid-state laser is used to produce a well-collimated light beam of single Gaussian mode having diffraction-limited divergence and a beam diameter of about 0.75 mm. Either the laser or an intermediate mirror is mounted on a single-axis translation mount and light is then directed toward a suitable-focal-length lens, which for convenience should be on a moveable mount. After passing through the lens, light is then reflected from another mirror (attached to a kinematic mount to enable easy adjustment) toward a quartz prism that is oiled (using objective lens immersion oil) onto a quartz microscope slide. Because the evanescent field is on the side of the slide opposite to that of the objective lens, use of 5- μm beads as spacers means that the coverslip can be closely opposed to the microscope slide. (b) For the small-angle case (i.e., low numerical aperture system), when a Gaussian laser beam is brought to a focus, the diffraction-limited spot size, ω_0 , is given by $f\lambda/d$, where f is focal length of the lens, λ is optical wavelength, and d is beam diameter. In our experiments $d = 0.75$ mm, $f = 160$ mm, $\lambda = 488$ nm, and spot size ≈ 100 μm , which gives a suitable area of illumination (using 100 \times objective lens power). (c) To adjust the TIR angle, either the laser or the mirror (see a) is translated. Since the specimen is at the focus of the lens, the spot remains in the same position but the input angle is altered by the translation of the laser or the mirror. Note that the range of adjustment, θ , is given by $\arctan(D/f)$, where D is the lens diameter, and the input angle divergence, ϕ , is given by $\arctan(d/f)$. For our system, $D = 25$ mm, so $\theta = 10^\circ$ and $\phi = 0.3^\circ$; this means that we can adjust the TIR angle over a reasonable range (θ) and the divergence of the input beam (ϕ) for any given setting is suitably small.

exceeds the critical angle for the glass–cytoplasm interface ($\approx 65^\circ$, since $n_{\text{glass}} = 1.5$, $n_{\text{cyto}} = 1.36$). Lenses with NA of less than 1.5 also have the advantage that conventional immersion oils and glass coverslips can still be used. The angle of incidence of the laser beam can be adjusted either by moving a mirror or a lens as shown in Figs. 3a and b, respectively.

3. Description of the equipment

3.1. Microscope

For the cell imaging experiments described here we used an objective lens-coupled TIRFM based on a Zeiss inverted microscope (Axiovert 100TV; Zeiss, Germany). A custom-built holder with two small (3-mm-diameter)

round mirrors mounted at 45° to the microscope axis was positioned in the slot in the objective turret, underneath the objective lens, normally used for insertion of the DIC Wollaston prism carrier (Fig. 4). We used a Zeiss Fluor 100 \times 1.45 NA objective lens and Zeiss low-fluorescence, 1.51 refractive index immersion oil.

3.2. Laser

We used an argon ion, all lines, TEM 0,0, single-mode laser (532-AP-A01; Melles Griot, CA, USA), which had an output of up to 50 mW at 488 nm, less than 2 mrad divergence (i.e., diffraction-limited output), and reasonable (<100 μrad) beam pointing stability. Leakage of other laser lines (e.g., 515 nm) was excluded using an externally mounted, 488-nm laser line, band-pass filter (e.g., XL06; Omega Optical, Brattleboro, VT,

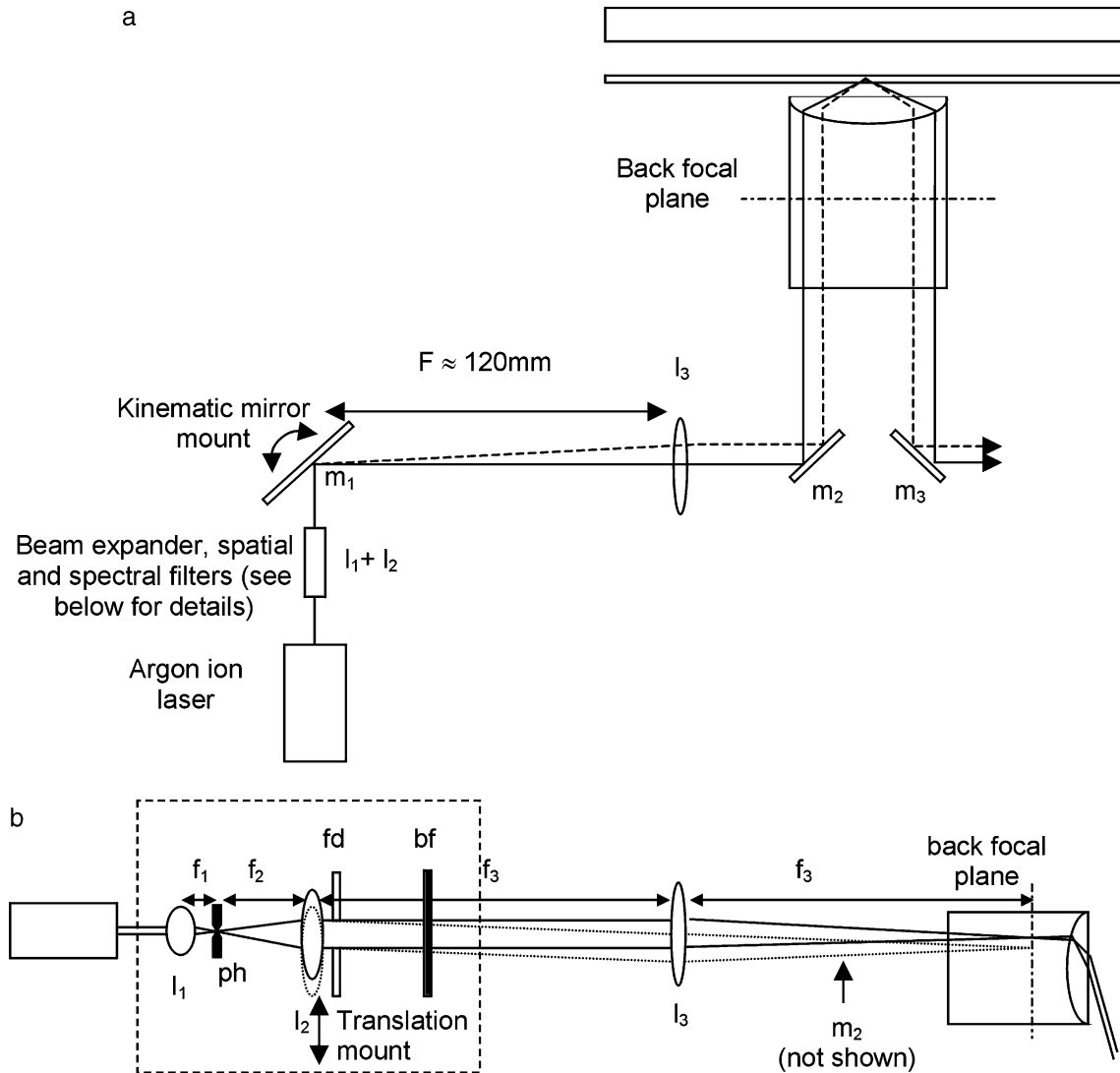


Fig. 3. Objective lens-coupled TIR microscopy. Laser light is focused at the outer edge of the back aperture of a high-numerical-aperture objective lens. In this peripheral region of the lens, light that enters strikes the glass–water interface at greater than the critical angle, is totally internally reflected at the interface, and then goes back to the opposite side of the objective lens. The laser beam is coupled into and out of the objective lens using either solid mirrors ($m_2 + m_3$) or a dichroic filter. Two methods of adjusting the input angle are shown. In (a), we see how the lens, l_3 , allows rotation of a mirror (m_1) mounted on a kinematic mount positioned at the focal distance to be used to change the TIR angle. In (b), we see how by translating a lens, l_2 (which is part of the beam expansion optic shown boxed in (a) for clarity), the input angle can also be adjusted. In (b) we see the light path in more detail and how the exciting laser light is “cleaned” by use of spatial and spectral filters (pin hole (ph) and barrier filter (bf)). Note that the TIR spot size at the object plane depends on the beam diameter at the conjugate plane, l_2 . A field diaphragm, fd , inserted close to the lens, l_2 , is used to control the size of the illuminated region.

USA). The cooling fan was mounted away from the optical table to prevent mechanical noise causing fluctuations in the beam angle (and hence TIR angle). The laser illumination levels were controlled via an RS232 interface, a custom-built mechanical shutter system that opened or closed within 10 ms, and the addition or subtraction of neutral-density filters.

3.3. Optical table

All optical components, including laser and microscope, were mounted on a vibration-isolated worksta-

tion (“VH workstation;” Newport, Irvine, CA, USA). A rail-mounted optical component system (see above) was used to construct the optical circuit (see Fig. 3).

3.4. Optical circuit

A Newtonian beam expander ($f = 10$ and $f = 160$) was constructed to produce a collimated, expanded laser beam (of ca. 12 mm diameter). A 50- μ m-diameter pinhole accurately positioned at the intermediate focus of the beam expander produced spatial filtering by removing higher-order scattered light. A laser-line band-

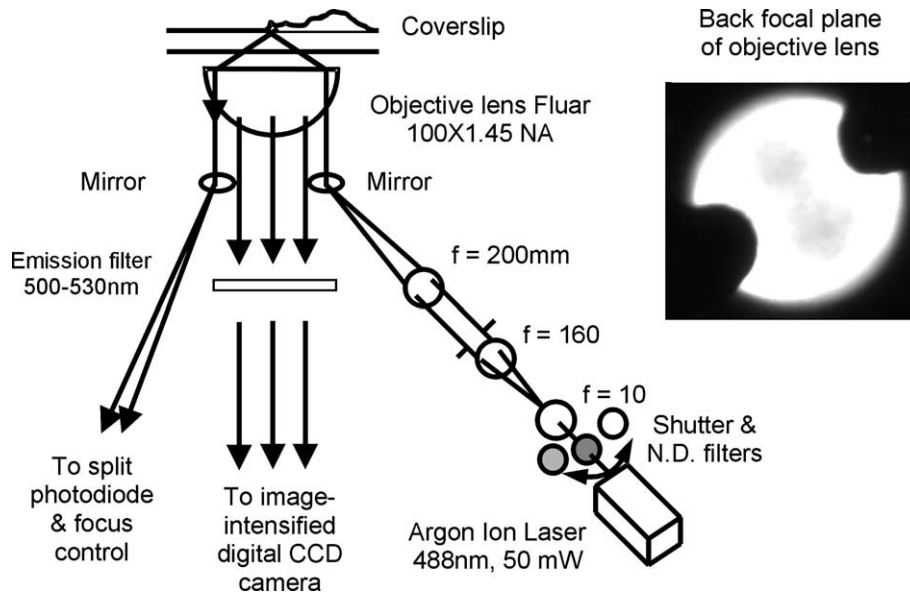


Fig. 4. Optical scheme of the objective-type TIRFM setup. The apparatus is based around a Zeiss inverted microscope (Axiovert100TV). Laser excitation is provided by an argon ion laser that is directed through a custom optical circuit (see Fig. 3) toward the Zeiss DIC slider insert aperture in the microscope nosepiece assembly. At this point, two round (3-mm-diameter) mirrors angled at 45° incidence are positioned at the extreme edges of the back aperture of the objective lens (Fluar, 100 \times , 1.45 NA; Zeiss) mounted in a custom-built holder. One of these mirrors directs the incoming laser beam toward the specimen and the other couples the returning, internally reflected beam out of the microscope (shown on schematic left and as mirrors m_2 and m_3 in Fig. 3). The angle of the exiting beam is used to servocontrol the system focus.

pass filter, inserted after the beam expander, improved spectral purity. Finally, a field diaphragm placed immediately after the beam expander enabled the size of the final TIR spot (at the specimen plane) to be controlled. *Translation* of the final lens ($f = 160$ mm) in the (x, y)-plane enabled the angle of incidence of the TIR spot to be changed without affecting the spot position (see Fig. 3b). *Translation* of this lens in the z -plane (in the direction of light propagation) focused the final beam. This was adjusted so that the beam exiting the microscope objective lens (see further details) was “best collimated.”

After passing through the beam-expansion and filtering optics, the laser beam was reflected from a plane mirror mounted on a kinematic mount. This was 200 mm from a third lens ($f = 200$ mm) which itself was a further 200 mm from the back focal plane of the objective lens. *Tilting* of the mirror again allowed the TIR angle to be adjusted without affecting spot position. *Translation* of the lens in the (x, y)-plane enabled spot position to be adjusted without greatly affecting the TIR angle.

To align the beam the bright-field lamp is switched on so that light enters the objective lens and is then reflected from the custom-built TIR mirrors. Optical components (see above) are then inserted, one by one, so that the light coming from the objective follows an undeviated path. This procedure ensures that all the components are correctly aligned with the microscope axis. When the laser is then switched on it should

retrace the same path and be approximately in the correct alignment. Fine adjustments are then made so that the laser beam is emitted from the front lens of the microscope objective. At this point the laser beam will be approximately collimated and will be emitted at an unspecified angle, presenting possible danger to the experimenter. Hence, it is advisable to wear suitable goggles (Glendale, Lakeland, FL, USA) at all times.

To optimize beam collimation, project the exiting beam onto the ceiling (if an inverted microscope is used) or onto a piece of card (if an upright microscope is used). Then, by z translation of the second beam expansion lens, the beam can be brought to “best collimation” and x - y translation of the same lens or tilting of the mirror causes the exiting beam angle and hence the TIR angle to change when the specimen is in place. This should be adjusted until the beam exits the lens at about 10° to the horizontal (80° incident angle). Then, when the specimen (e.g., glass slide + water medium) is mounted, the beam angle should reach the critical angle for the glass–water interface (61.5 – 62°) and should no longer exit the lens but, instead, should reflect back from the coverslip–water interface and be coupled out of the microscope on a path roughly parallel to that of the input beam by the second mirror positioned at the back focal plane. As a control specimen we suggest use of a dilute solution (0.05% W/V) of 500-nm-diameter, yellow–green-fluorescent latex beads (Bang’s Laboratories, Fishers, IN, USA).

3.5. Camera

We used a digital CCD camera coupled to a two-stage, multichannel-plate image intensifier (*GemStar*; Photonic Science, Millham, UK). The entire system (camera + intensifier) was computer controlled and data transfer was digital at 10- or 12-bit resolution. The ability to change parameters such as exposure time, pixel binning, region of interest, intensifier gain, and CCD camera gain has the drawback that there are many different overall gain settings and signal-to-noise ratios. After systematically measuring the signal-to-noise ratios at different gain combinations on control specimens in our system, we optimized settings for the best signal-to-noise at a gain appropriate for identification of single fluorophores at a given frame rate. Unfortunately, no camera manufacturer that we know provides full details for each camera made and their individual properties vary quite widely. Therefore, experimentation is required for any camera system used. Technology is changing fast in this area and it is likely that low-noise, cooled CCD cameras will shortly be the best option for single-molecule observation.

3.6. Computer hardware and software

A proprietary digital frame-grabber (*Snapper*; Data-Cell, UK) was used to control the camera and capture data at acquisition rates of 20 Mpixel s⁻¹. We found modern IBM-PC type computers (Pentium III, 1 GHz or better) to be fast enough for simultaneous real-time image display, hard drive recording (at a maximum speed of 15 Mpixel s⁻¹), and off-line image analysis.

No commercial software to record and analyze data at sufficient speed or capacity (30 Mbytes s⁻¹ and up to 500 Mbytes per record) was available, so we developed our own software. A copy of the single-molecule image analysis package “YorkView” and examples of data files can be obtained at <http://motility.york.ac.uk>. The computer program controls all of the microscope, camera, laser, and moveable optical components and stores all settings, together with other experimental parameters, with each data sequence. This information is crucial for the subsequent automated image analysis routines (described below).

4. Experimental procedures

4.1. Production of GFP fusion constructs

We used eGFP and eGFP fused to proteins of interest in our experiments. In general, primers flanking the gene of choice should be produced so that resulting DNA fragments can be subcloned into PeGFP-N1 and peGFP-C1 (BD Biosciences Clontech, Palo Alto, CA,

USA), to create the required GFP fusion construct that is in-frame and at either the N or the C terminus. To check that cloning has been successful, constructs can be transiently expressed in *COS* cells and the cell lysates immunoblotted, using an anti-GFP antibody (Abcam, Cambridge, UK), to confirm that the expressed proteins are of the correct size.

4.2. Cell culture and transfection

Here we have used mouse myoblast cells that were isolated from the “immortal mouse” (h2k^b-tsA58) and cultured as described [22]. These were transfected using FuGene-6 (Roche Diagnostics, Basel, Switzerland) following the recommended protocol. After 24 h, the cells were plated onto glass coverslips and allowed to settle. Eight hours later, the medium was replaced with Hanks’ balanced salt solution containing 20 mM Hepes (pH 7.4) without serum, and the coverslip was assembled into a small chamber for viewing the cells on the inverted microscope. Expression levels were quantified from confocal images of the cells that were compared with control dilutions of GFP in the same buffer (Fig. 5).

By adjusting the above transfection procedures it was possible to ensure that about 10% of the cells in a given culture had suitable levels (approx 10 nM) of expression for TIRF measurements. To view the cells it was important to use a bathing medium that had low autofluorescence. Single GFP-tagged molecules could then be identified above the background noise at the basal plasma membrane of the leading lamella (Fig. 6).

Control coverslips, which were sparsely decorated with single GFP fluorophores, were created by incubating the coverslip with a low concentration of anti-GFP antibody, blocking with 1 mg/ml bovine serum albumin, and then incubating with a solution of about 10 nM GFP. Coverslips were then viewed using TIRFM. Individual GFP fluorophores could be identified as separate objects that exhibited either one- or two-step photobleaching (Fig. 7). These control slides were important in setting up the TIRFM apparatus and in establishing single-fluorophore sensitivity.

4.3. Single-fluorophore observation and detection

To analyze the behavior of single fluorophores inside living cells, we wrote an automated single-fluorophore-detection computer program that passed temporal and spatial information about each identified fluorophore to further analysis programs. We called this module of the program the single-fluorophore detection algorithm (SFDA). To discriminate single fluorophore behavior from noise and avoid false-positive detection we defined four criteria, **D.I.S.H.**, that must be satisfied. The fluorescent image must (1) be diffraction-limited in size, (2)

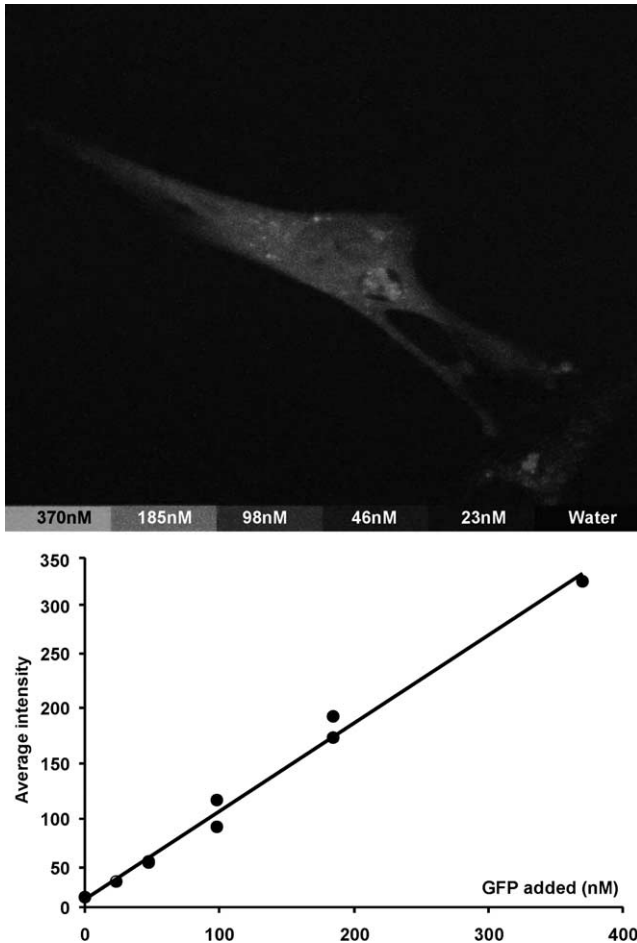


Fig. 5. Determination of GFP-fusion protein expression levels in transiently transfected mouse myoblast. Cells were cultured on glass coverslips and transfected using the Fugene system (see text for details). Cell images, taken using a confocal microscope (Pascal LSM; Zeiss), were compared to those obtained using the same exposure and image collection parameters of control dilutions of pure GFP solution (top image with lower inserts). GFP expression level was determined from the mean cellular fluorescence compared to the GFP standard calibration graph (bottom). The cell shown here is expressing about 125 nM GFP (about five molecules per diffraction-limited optical volume) and is shown for clarity of illustration. (Cells used for single-fluorophore TIRFM imaging had about 10 times lower expression levels than this.)

have intensity corresponding to that of a single fluorophore (measured under controlled conditions), (3) show single-step photobleaching and (4) have a half-life proportional to the illumination intensity (i.e., the rate of disappearance depends upon the illumination intensity). During analysis every pixel in the entire data set is analyzed and contributes to 25 different runs of 5×5 pixel matrices ($0.16 \mu\text{m}^2$ area). Each temporal trajectory of intensity, determined from the sum of each given diffraction-limited region, is searched for single-step disappearance or appearance of intensity approximately equal to that of a known single fluorophore. Data sets

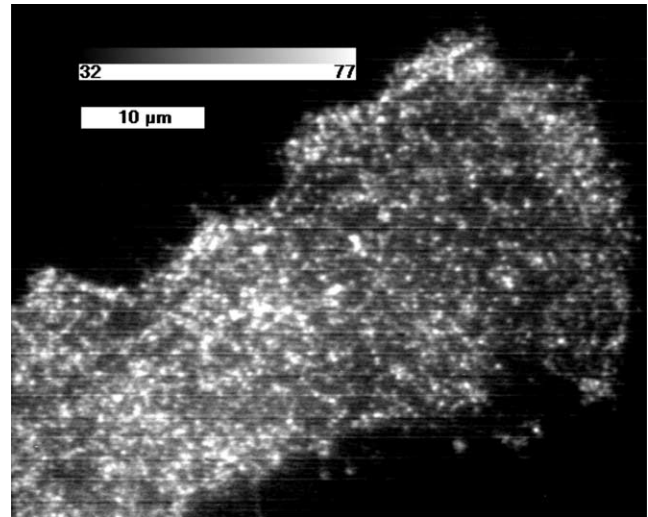


Fig. 6. Fluorescence of individual GFP molecules bound to the leading lamellar, plasma membrane of a living mouse myoblastic cell that had been transiently transfected with a Myosin X PH domain–GFP fusion protein construct. The individual fluorescent spots obey the DISH criteria: diffraction-limited spot size, intensity appropriate to single fluorophore, single-step photobleaching, and half-life dependent on incident laser power (see text for details).

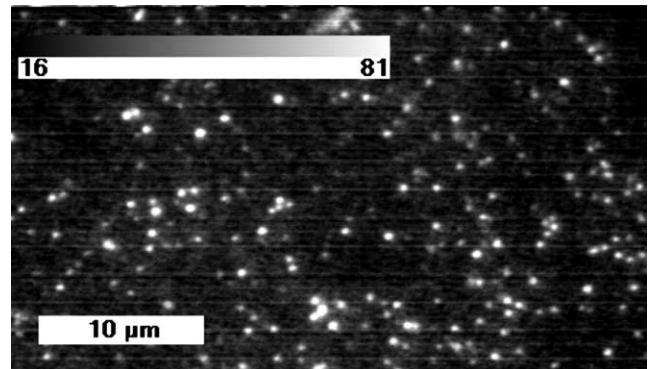


Fig. 7. TIRFM image of GFP molecules bound to anti-GFP antibodies on glass surface. Some spots have double intensity either because the antibody binds two GFP molecules or because of the tendency for GFP to dimerize.

obtained at different laser powers are then compared to ensure that the lifetime of the identified objects depends upon incident laser power.

SFDA consists of a three-pass computer algorithm. On the first pass of the algorithm, the intensity of a diffraction-limited area (5×5 pixels, $0.16 \mu\text{m}^2$) around each center pixel is running-averaged over time through separate image frames. The time-series intensity data are then tested for single-step bleaching behavior, whereby the intensity over a section of the data must show a significant change in intensity (by a running Student t test statistic) that is similar in amplitude to that of a single fluorophore. All center pixels that show such

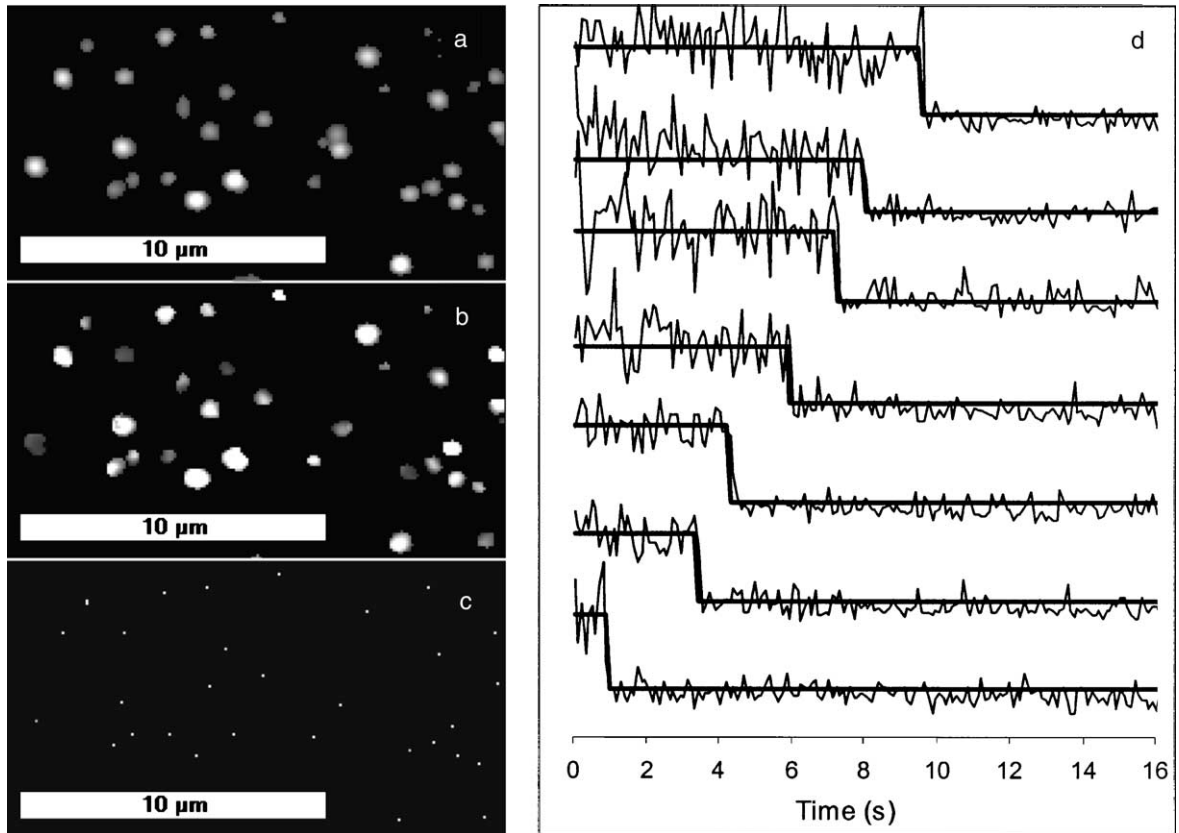


Fig. 8. Single-fluorophore, three-pass detection algorithm. The sample consisted of GFP molecules immobilized on a glass surface (similar to Fig. 7) (a) Pass one: each 5×5 matrix of pixels ($0.16 \mu\text{m}^2$) is tested for the biggest intensity drop occurring in each 5×5 pixel region; this gives the “drop image” mask. (b) Pass two: each unconnected diffraction-limited single-step bleaching region is identified. (c) Pass three: the centroid of each identified single fluorophore is calculated and the final reduced output data set is written to the temporal and spatial trajectory arrays. (d) Intensity trajectories of sample individual fluorophores are shown together with their calculated idealized behaviors (solid fitted lines). Fluorescence data were collected at 10 frames/s.

single-step rises or falls in intensities of correct amplitude are then stored and used as a mask to restrict further analysis to those candidate regions only (Fig. 8a).

On the second pass, the intensity immediately before and after each photobleaching event is determined by averaging the signal over an interval of about 250 ms before and after the step change in intensity (fitted lines on Figs. 5 and 8d). Adjacent clusters of pixels are tested to ensure that each identified object is of the correct size and amplitude. Objects larger than the known diffraction-limited size or of incorrect intensity amplitude are rejected at this point (Fig. 8b).

On the third pass, the center position of each object is calculated using a least squares algorithm to determine the centre of mass. The final, reduced-output data series contains the temporal and spatial data derived from the sum of the output (temporal and positional) derived for each identified single fluorescent object (Figs. 8c and d). Information about fluorophore intensity, times of appearance and disappearance, total life-

time, and positional coordinates (x, y against time) can then be extracted. This information is used to plot the population fluorophore intensity distribution, lifetime distribution, landing rate, inter fluorophore distance, and so on. Currently, our estimates of fluorophore position are accurate to about 100 nm and lifetimes to about 100 ms.

Using the above algorithm, the trajectory of individual fluorophores can be extracted as raw data and compared to fitted lifetimes to check that the results appear “reasonable” (e.g., see fitted lines in Fig. 9). Notice that data from control slides consisting of GFP bound to anti-GFP antibody (Fig. 8) are slightly “cleaner” than data from living cells (Fig. 9). Nevertheless, the data are extremely similar in overall appearance. Amplitudes, lifetimes, and bleaching times are all similar. Data obtained from cells also show a characteristic decay at the start of each record due to bleaching of the cellular autofluorescence background. Note that this is a smooth decay because many weakly fluorescent molecules contribute to the signal.

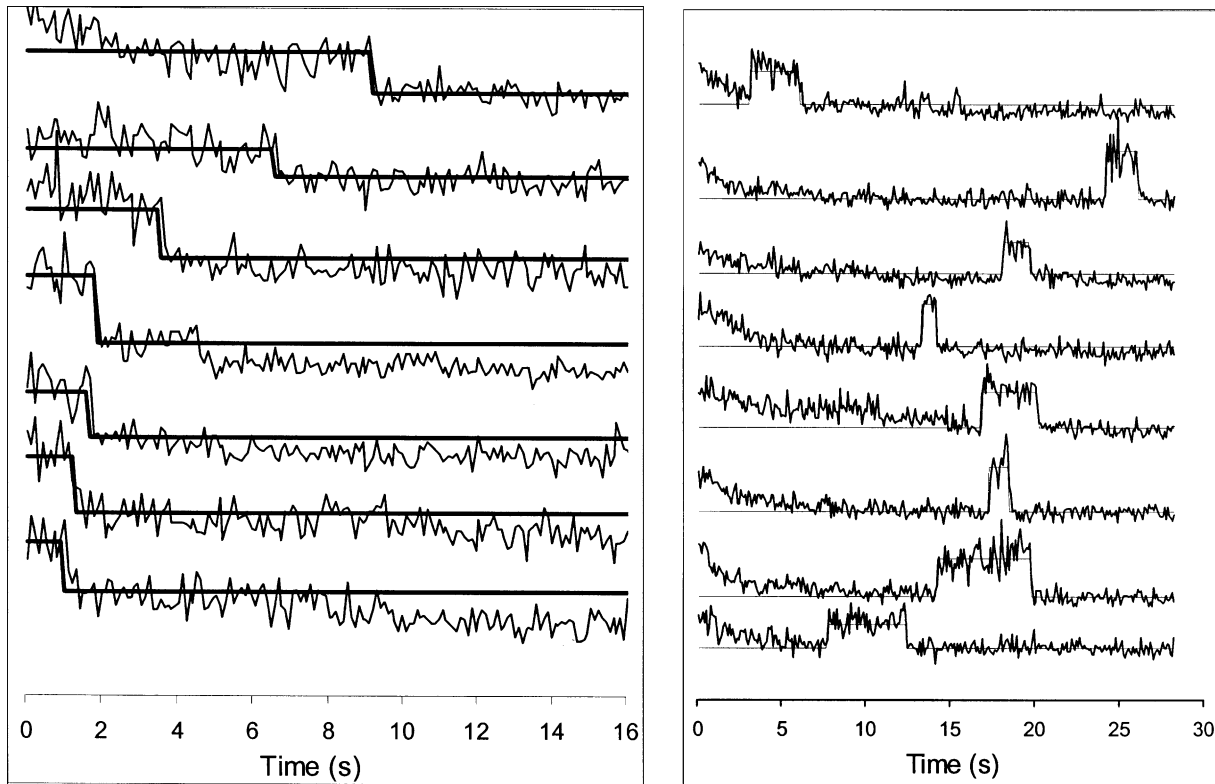


Fig. 9. (Left) Fluorescence intensity trajectories for single GFP–myosin \times pleckstrin homology domain fusion protein molecules bound to basal plasma membrane. Fluorescent signal collected from diffraction-limited areas (5×5 pixels, $0.16 \mu\text{m}^2$) at 10 frames/s rate. (Right) As on the left, but here we see trajectories for fluorophores that arrive and depart during the course of the experiment. Note the background fluorescence bleaching at the start of each record but otherwise good similarity to control, GFP on glass, data sets (Fig. 8).

4.4. Troubleshooting

(1) Correct laser beam alignment is critical for TIRFM to work and we suggest removal of optical components one by one from the light path to check that the positions of the optical components in the light path are coaxial and that each produces either minimal deviation or the intended deviation in the light path.

(2) Coverslips should be made from low-autofluorescence glass (e.g., “extra-white” glass), fused silica, or quartz (note that quartz has a significantly lower refractive index and therefore a higher angle for total internal reflection fluorescence). Note that objective lenses have low aberrations only if the correct optical thickness of coverslip and immersion oil are used.

(3) Laser emission should be carefully checked for the presence of other laser lines. Even 0.1% of contaminant longer-wavelength emission (e.g., 515 nm) would make GFP detection impossible. If this is the case then narrow bandpass or laser line filters should be used.

(4) Vibration isolation is important because even tiny fluctuations in the angle of the incident beam affects fluorescence amplitude and interferes with subsequent automatic detection.

(5) Further information can be obtained at <http://motility.york.ac.uk/>.

Acknowledgments

We thank the BBSRC, The Royal Society (London), and the Wellcome Trust for support.

References

- [1] T.A. Byassee, W.C.W. Chan, S.M. Nie, *Anal. Chem.* 72 (2000) 5606–5611.
- [2] G.S. Harms, L. Cognet, P.H.M. Lommerse, G.A. Blab, T. Schmidt, *Biophys. J.* 80 (2001) 2396–2408.
- [3] G. Jung, J. Wiehler, B. Steipe, C. Brauchle, A. Zumbusch, *Chemphyschem* 2 (2001) 392–396.
- [4] T. Kues, R. Peters, U. Kubitscheck, *Biophys. J.* 80 (2001) 2954–2967.
- [5] R. Iino, I. Koyama, A. Kusumi, *Biophys. J.* 80 (2001) 2667–2677.
- [6] W.E. Moerner, E.J.G. Peterman, S. Brasselet, S. Kummer, R.M. Dickson, *Cytometry* 36 (1999) 232–238.
- [7] Y. Sako, S. Minoghchi, T. Yanagida, *Nat. Cell Biol.* 2 (2000) 168–172.
- [8] G. Seisenberger, M.U. Ried, T. Endress, H. Buning, M. Hallek, C. Brauchle, *Science* 294 (2001) 1929–1932.

- [9] D. Toomre, D.J. Manstein, *Trends Cell Biol.* 11 (2001) 298–303.
- [10] M. Ueda, Y. Sako, T. Tanaka, P. Devreotes, T. Yanagida, *Science* 294 (2001) 864–867.
- [11] B. Ludin, A. Matus, *Trends Cell Biol.* 8 (1998) 72–77.
- [12] D.C. Prasher, V.K. Eckenrode, W.W. Ward, F.G. Prendergast, M.J. Cormier, *Gene* 111 (1992) 229–233.
- [13] R.M. Dickson, A.B. Cubitt, R.Y. Tsien, W.E. Moerner, *Nature* 388 (1997) 355–358.
- [14] R. Heim, D.C. Prasher, R.Y. Tsien, *Proc. Natl. Acad. Sci. USA* 91 (1994) 12501–12504.
- [15] A. Volkmer, V. Subramaniam, D.J. Birch, T.M. Jovin, *Biophys. J.* 78 (2000) 1589–1598.
- [16] G.S. Harms, L. Cognet, P.H.M. Lommerse, G.A. Blab, H. Kahr, R. Gamsjager, H.P. Spaink, N.M. Soldatov, C. Romanin, T. Schmidt, *Biophys. J.* 81 (2001) 2639–2646.
- [17] M.F. Paige, E.J. Bjerneld, W.E. Moerner, *Single Mol.* 2 (2001) 191–201.
- [18] D. Axelrod, *Traffic* 2 (2001) 764–774.
- [19] D. Axelrod, in: J.R. Lakowicz (Ed.), *Topics Fluoresc. Spectrosc.*, 3, Plenum Press, New York, 1992, pp. 289–342.
- [20] A.L. Stout, D. Axelrod, *Appl. Optics* 28 (1989) 5237–5242.
- [21] T. Funatsu, Y. Harada, M. Tokunaga, K. Saito, T. Yanagida, *Nature* 374 (1995) 555–559.
- [22] P. Clark, D. Coles, M. Peckham, *Exp. Cell. Res.* 230 (1997) 275–283.